RKKY coupling in Weyl semimetal thin films

Sonu Verma, Debasmita Giri, H. A. Fertig, and Arijit Kundu

Phys. Rev. B **101**, 085419 — Published 24 February 2020

DOI: 10.1103/PhysRevB.101.085419

RKKY coupling in Weyl semimetal thin films

Sonu Verma,[1] Debasmita Giri,[1] H.A. Fertig,[2] and Arijit Kundu[1]

[1] *Department of Physics, Indian Institute of Technology Kanpur, Kanpur 208016, India*
[2] *Department of Physics, Indiana University Bloomington, Bloomington 47405, USA*

We consider the effective coupling between impurity spins on surfaces of a thin-film Weyl semimetal within Ruderman-Kittel-Kasuya-Yoshida (RKKY) theory. If the spins are on the same surface, their coupling reflects the anisotropy and the spin-momentum locking of the Fermi arcs. By contrast when the spins are on opposite surfaces, their coupling is mediated by the Fermi arcs as well as by bulk states. In this case the coupling is both surprisingly strong and highly thickness dependent, with a maximum at an optimum thickness. We demonstrate our results using analytical solutions of states in the thin-film geometry, as well as using a two-surface recursive Green's function analysis of the tight-binding model.

I. INTRODUCTION

Weyl semimetals (WSMs) are three dimensional topological systems that host an even number of band-touching points (termed as *Weyl nodes*) in the bulk spectrum, near which the low-energy excitations follow the relativistic Weyl equation[1]. Such Weyl quasiparticles have definite chirality, and the chirality of these quasiparticles are given by the nature of the Weyl nodes, which can act as either sources or sinks of Berry curvature in the Brillouin zone. In a finite geometry, WSMs also host unique surface states known as *Fermi arc* states, whose projected Fermi surfaces are open arcs on each of the surfaces. Numerous materials have been predicted to be suitable candidates for WSMs , and a variety of experiments demonstrate their novel character.

Correlations functions impact many properties of these systems, and are of special interest because of the unique helical nature of low-energy excitations in WSMs. Within this class of properties, the effective interaction between two localized impurity spins introduced in such a system, mediated by the WSM conduction electrons, is described by the Ruderman-Kittel-Kasuya-Yoshida (RKKY) theory[2], and is directly related to the spin-spin correlation function of electrons within the system. Among solid-state materials, spin-orbit coupled systems [3,4], particularly topological and Dirac systems, are interesting in the way they mediate long-range – and sometimes controllable – coupling[5–17] among spins. Work on RKKY interactions through bulk Weyl fermions[18–20] show the interactions can be anisotropic and are in some circumstances weak, but generally carry signatures of the chiral nodes.

Significant attention has also been given to RKKY interactions on the surface of WSMs[21–23]. Surface states, at the Fermi energy of a WSM in a slab geometry, typically reside at wavevectors which form arcs in the surface Brillouin zone. These arcs join one Weyl node to the other, and typically disperse energetically perpendicular to a given arc, with different signs of the dispersion for each of the two physical surfaces. The essentially one dimensional character of the surface states results in a strong, highly anisotropic spin-spin correlation function, with similarly anisotropic RKKY interactions among spin impurities adsorbed on the surface of a WSM. Previous studies have been largely confined to semi-infinite geometries, for which coupling *between* surfaces cannot be modeled. Such coupling is potentially significant, as the Fermi arc states can be relatively weakly localized at their surfaces; moreover, the penetration length of a Fermi arc state diverges as the surface wavevector approaches the projection of a Weyl node. This can induce interesting physics due to non-negligible coupling between spins on opposite surfaces of the WSM.

In this paper, we investigate the effects of such inter-surface coupling by analyzing a slab geometry of finite thickness. Specifically, we examine effective spin-spin interactions due to the RKKY mechanism for two different situations. Firstly, when two spins are on the *same* surface of the WSM, surface electrons on the opposite surface can participate in their coupling. The resulting RKKY interaction reflects the anisotropy of the Fermi surface, and in the thick slab limit can be compared with previous results in which only a single surface was modeled[21]. Secondly, when the spin impurities are on *opposite* surfaces of the slab, the resulting coupling depends strongly on the overlap of the Fermi arc states. We find that the resulting coupling is a non-monotonic function of the slab thickness, and a thin-film limit can be defined by observing when the coupling between the spins is strongest. In order to compute the coupling, we have developed a recursive Green's function scheme in which the elements of a Green's function on the surfaces can be computed essentially exactly with relatively high numerical efficiency. We show that analytical solutions for the WSM wavefunctions in a slab geometry agree with the numerical results, and offer some qualitative insight into their behavior.

This manuscript is organized as follows. In Section II, we introduce the simple WSM model used for our work and find analytical solutions for wavefunctions in a slab geometry with appropriate boundary conditions. In Section III, we briefly discuss the formal expression for RKKY interactions and our numerical scheme for computing them in a slab geometry of a tight-binding model. Our numerical results along with their asymptotic behav-

iors are presented in Section IV, where we make comparison with analytical results. Finally we conclude with a summary and discussion in Section V.

II. WEYL SEMIMETAL - THIN FILM

A. Model Hamiltonian

A minimal model of a WSM has two Weyl nodes at the Fermi energy and breaks time-reversal (TR) symmetry. For such a model, the low-energy Hamiltonian can be written using a two-band model. If the two bands represent spin states, then for a slab geometry, with the Weyl nodes separated along the momentum of one of the translational invariant (in-plane) directions, the surface states (Fermi arcs) are spin-polarized, resulting in completely spin-polarized surfaces of the slab. As the indirect spin-exchange interaction is only interesting when the ground-state is spin-*unpolarized*, the minimal model we consider must have at least two Fermi arcs on each surface, with the spin-polarizations of each oriented such that the net spin density on either surface vanishes. If the two Fermi arcs on a surface have distinct locations in the surface Brillouin zone, then one has a total of four Weyl nodes in the bulk, each with a distinct location in momentum space. If the Fermi arcs join two *Dirac* nodes, then the Fermi arcs will overlap in the surface Brillouin zone. This latter situation was considered, for example, in Ref. 21. In our work we confine our studies to the former case (i.e., Weyl semimetals).

Our starting point is a model Hamiltonian defined on a cubic lattice[24]. The Hamiltonian preserves time-reversal symmetry (defined by the time reversal operator $T = i\sigma_y K$, with K the complex conjugation operator and σ_y a Pauli matrix acting in the spin-space), but breaks inversion symmetry, and so has four degenerate Weyl nodes. Specifically, we take

$$H(k) = \lambda \sum_{\alpha=x,y,z} \sigma_\alpha \sin k_\alpha - \mu + \tau_y \sigma_y M_k. \qquad (1)$$

Here $M_k = m + 2 - \cos k_x - \cos k_z$, and τ_α are Pauli matrices acting in an orbital space. For $|m| \leqslant \lambda$ the four Weyl nodes are located at $\boldsymbol{k} = (0, \pm\pi/2 \pm k_0, 0)$, where $k_0 = \pi/2 - \sin^{-1}(m/\lambda)$ (with lattice spacing a our unit of length and $\hbar = 1$). On a given surface, the two Fermi arcs join the four Weyl nodes in a pairwise fashion, as illustrated in Fig. (1). States of the two Fermi arcs are spin-polarized along σ_x in opposite directions (i.e, they are eigenvectors of $\sigma_x \equiv \tau_I \otimes \sigma_x$ with opposite eigenvalues for the two Fermi arcs). Furthermore, the two Fermi arcs, at low-energy, are dispersionless along the k_y direction and have opposite velocities along the x direction.

The Hamiltonian can be brought into a block diagonal form. Writing $H' = UHU^\dagger$, with the unitary matrix U

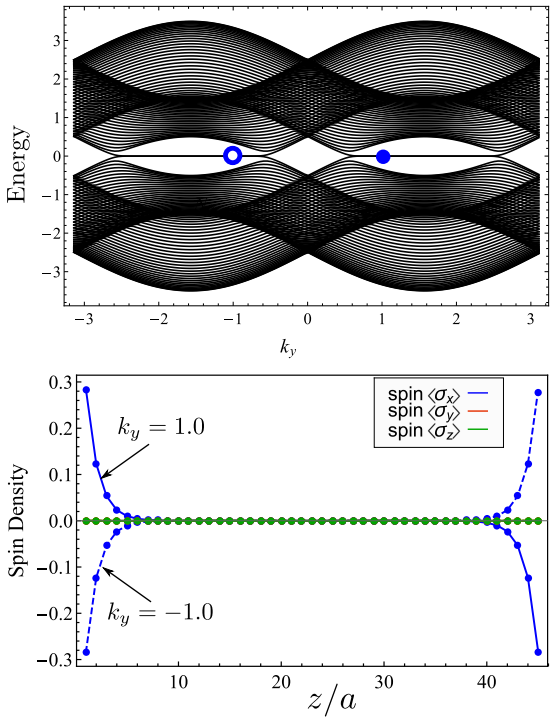

FIG. 1. Top: For the WSM, Eq. (1), in a slab geometry with finite thickness in z direction and for $k_x = 0$, the band-structure (in the units of λ) as a function of k_y shows the four Weyl nodes in the bulk, with the two Fermi arcs joining them. (The lattice spacing a is taken to be unity). Bottom: The spin densities of the Fermi arc states are shown as a function of z for two values of k_y as indicated in the top figure. Parameters: $m = 0.5\ \lambda$, thickness $N_z = 45$ lattice spacings.

defined by

$$U = \frac{1}{2}\begin{pmatrix} -1 & -i & -i & 1 \\ 1 & -i & i & 1 \\ 1 & i & -i & 1 \\ -1 & i & i & 1 \end{pmatrix}, \qquad (2)$$

one finds H' has two 2×2 blocks, where for each block (labeled by $\eta = \pm 1$), the two-band Hamiltonian is

$$H'_\eta = \lambda(\sigma_y \sin k_x - \sigma_x \sin k_z) + \eta\sigma_z(2 + m - \cos k_x - \cos k_z) - \lambda\sigma_z \sin k_y. \qquad (3)$$

This is a particularly useful form, in which each block individually breaks time-reversal (TR) symmetry, while T maps H'_+ to H'_- (and vice-versa), so that the total Hamiltonian is TR symmetric. Each of the blocks has two Weyl nodes separated in momentum space, and on a given surface they are joined by one Fermi arc. In principle, a system hosting many Fermi arcs on a surface should be structured in such a way that each joins two Weyl nodes; an effective model of such a multi-Weyl node system could be written as $H = H_1 \otimes H_2 \otimes \cdots$, where each of the blocks contains two Weyl nodes.

To focus on the physics of the Fermi arcs, we expand the Hamiltonian to lowest non-trivial order in k_x and k_z,

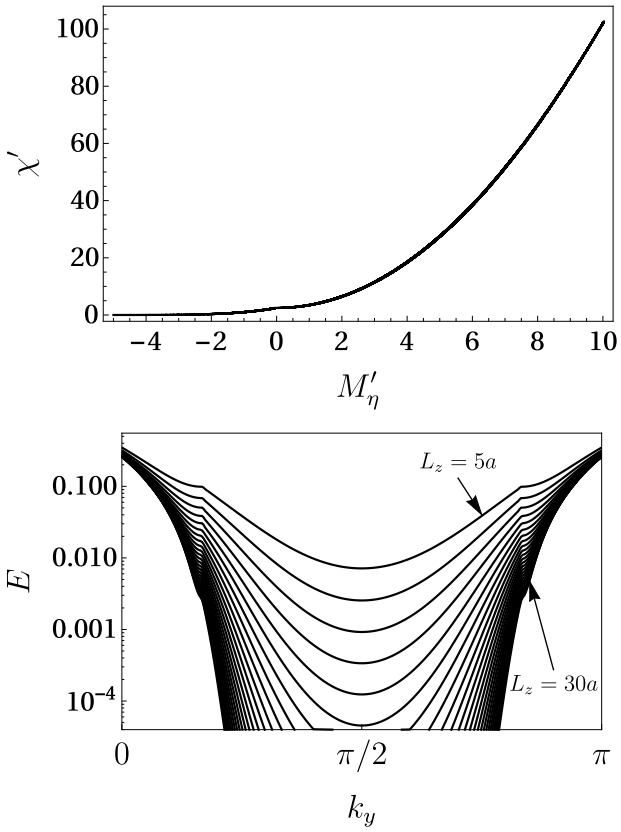

FIG. 2. (Top) Minimum solution of χ' for values of M'_η. When $M'_\eta \to -\infty$, $\chi' \to 0$, when $M'_\eta = 0$, $\chi' = (\pi/2)^2$ and for large M'_η, $\chi' \approx M'^2_\eta + \pi^2$. (Bottom) The lowest energy solution for $q_x = 0$ for various values of L_z from 5 to 30 are shown for half of the Brillouin zone, containing two Weyl nodes. The energy values decrease exponentially with increasing L_z, characteristic of surface states, for k_y between the Weyl nodes.

writing $k_x \to q_x$ and $k_z \to q_z$. Then from Eq. (3) we obtain

$$H'_\eta \approx \lambda(\sigma_y q_x - \sigma_x q_z) + \sigma_z M_\eta(k_y), \tag{4}$$

with $M_\eta(k_y) = m\eta - \lambda \sin k_y$. The four Weyl nodes are at $\mathbf{K}_{\eta,\xi} = (0, \eta\frac{\pi}{2} + \xi k_0, 0)$ with $\eta, \xi = \pm 1$ and $k_0 = \cos^{-1}(m/\lambda)$. For the $\eta = +1$ block, $M_+ < 0$ between $k_y \in (\pi/2 - k_0, \pi/2 + k_0)$. For a surface perpendicular to the z direction, along the k_y axis these two points are connected by a Fermi arc. For the $\eta = -1$ block, $M_- > 0$ between $k_y \in (-\pi/2 - k_0, -\pi/2 + k_0)$, and again there is a Fermi arc connecting these points on the k_y axis for the same surface. This situation is illustrated in Fig. 1. Note that for H' (i.e., after the unitary transformation), states on the Fermi arcs are eigenvectors of σ_y rather than σ_x.

Near the Weyl nodes, if we can write the low-energy Hamiltonian in the form of $H = k_\mu A_{\mu\nu}\sigma_\nu$, then the chirality of the node is given by $\mathrm{sgn}(\mathrm{Det}[\mathbf{A}])$. Writing $\boldsymbol{k} = (q_x, \eta\frac{\pi}{2} + \xi k_0 + q_y, q_z)$ and expanding to first order in q_i, we arrive at the low-energy Hamiltonian

$$H^{\mathrm{low}}_{\eta\xi} \approx \lambda(\sigma_y q_x - \sigma_x q_z) + \eta\xi\alpha\sigma_z q_y, \tag{5}$$

with $\alpha = \sqrt{1 - (m/\lambda)^2}$. The chiralities of the four nodes may then be written as $\mathrm{sgn}(\mathrm{Det}[\mathbf{A}_{\eta,\sigma}]) = -\eta\xi$.

B. Infinite mass boundary condition

To make progress analytically, we need to construct appropriate boundary conditions of the Dirac Hamiltonian Eq. (3) for a slab geometry, such that the properties of the Fermi arc can be recovered. In general boundary conditions for the Dirac equation can be cumbersome, but our goal here is to recover the properties of the surface modes (i.e, Fermi arc states). Thus we adopt relatively simple boundary conditions by taking the Hamiltonian of the vacuum (outside the slab, which extends from $z = 0$ to $z = L_z$), to be similar to Eq. (4), except for the mass term, whose form is taken as $M^{\mathrm{vac}}_\eta = \eta m_0$, with $m_0 \to \infty$. This construction is required to ensure that for momentum between the Weyl nodes the effective mass term ($M_\eta(k_y)$) for the Weyl semimetal and the vacuum (M^{vac}_η) are oppositely signed.

The eigenfunctions for the Hamiltonian $H_{\mathrm{vac}} = \lambda(q_x\sigma_y - q_z\sigma_x) + M^{\mathrm{vac}}_\eta\sigma_z$ are

$$\psi_{\mathrm{vac}} \propto \begin{pmatrix} \lambda(q_z + iq_x) \\ M^{\mathrm{vac}}_\eta - E \end{pmatrix} e^{i(q_z z + q_x x)}, \tag{6}$$

with eigenvalue $E = \pm\sqrt{m_0^2 + \lambda^2(q_z^2 + q_x^2)}$. For $m_0 \gg E$, the eigenfunctions are normalizeable if

$$q_z = i\kappa, \quad \text{for } z \geq L_z,$$
$$q_z = -i\kappa, \quad \text{for } z \leq 0,$$

with $\kappa = \sqrt{m_0^2 + q_x^2 - E^2}$. Thus, in the limit $m_0 \to \infty$, we have $\kappa \to m_0$. For $z > L_z$,

$$\psi_> \propto \begin{pmatrix} im_0 + iq_x \\ \eta m_0 - E \end{pmatrix} e^{-m_0 z} \approx \begin{pmatrix} i \\ \eta \end{pmatrix} e^{-m_0 z}. \tag{7}$$

For $z < 0$,

$$\psi_< \propto \begin{pmatrix} -im_0 + iq_x \\ \eta m_0 - E \end{pmatrix} e^{m_0 z} \approx \begin{pmatrix} i \\ -\eta \end{pmatrix} e^{m_0 z}. \tag{8}$$

At $z = 0$ and L_z, these spinors become the Fermi arc wavefunctions, and are recognizable as eigenvectors of σ_y.

Matching the wavefunction $\psi(z)$ within the slab to these boundary forms yields the conditions

$$\psi(z = 0) \propto \psi_<(z = 0) \ \text{ and } \ \psi(z = L) \propto \psi_>(z = L_z), \tag{9}$$

where

$$\psi(z) = a \begin{pmatrix} \lambda(q_z + iq_x) \\ M_\eta(k_y) - E \end{pmatrix} e^{iq_z z} + b \begin{pmatrix} \lambda(-q_z + iq_x) \\ M_\eta(k_y) - E \end{pmatrix} e^{-iq_z z}, \tag{10}$$

with $q_z = (1/\lambda)\sqrt{E^2 - M_\eta^2 - \lambda^2 q_x^2}$. Non-trivial solutions of Eq. 9 exists if

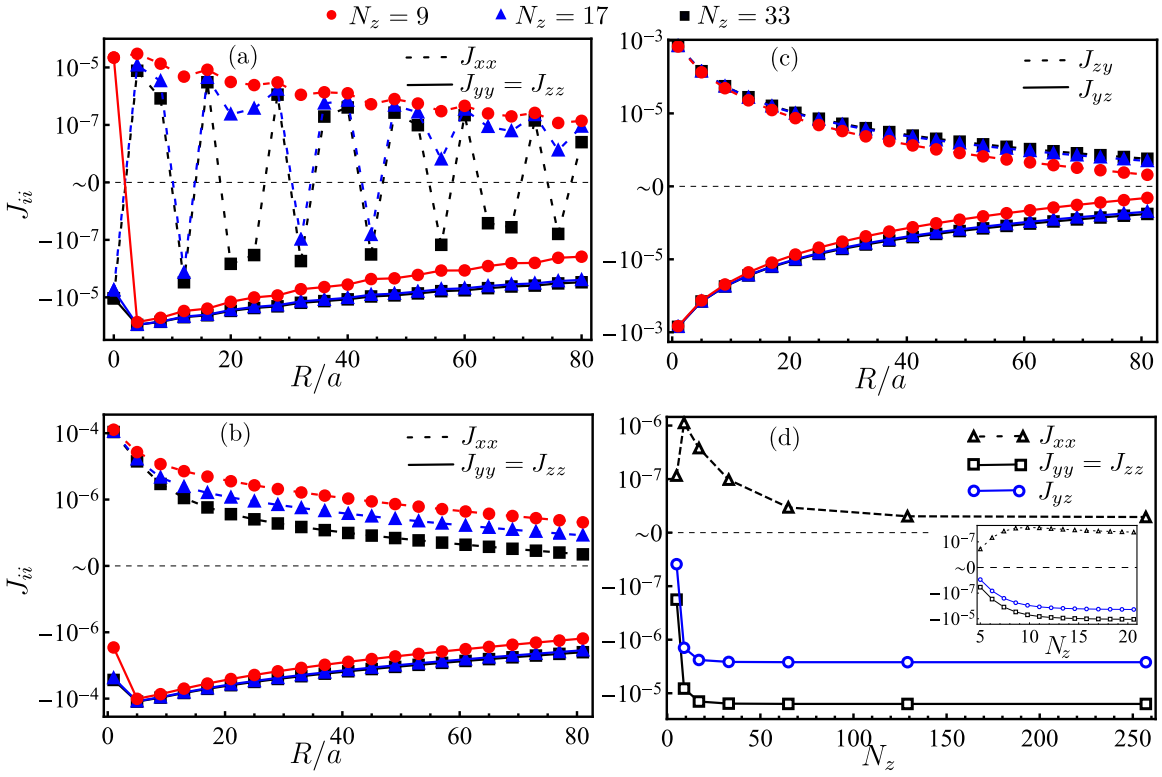

FIG. 3. The RKKY coupling between two spins (connected to the same orbital) put on the same surface (along x-direction *i.e.* $\mathbf{R} = (R, 0, 0)$) of the WSM slab with (a) the analytical wave-functions and keeping only the $n = 0$ bands, (b), (c) numerically evaluated Green's function in the real-space. With increasing thickness, the all components except J_{xx} becomes essentially thickness independent after certain thickness, as shown in (d). Inset of (d) shows the RKKY coupling vs slab thickness calculated using analytical wave-functions and $n = 0$ bands. Results shown are for $\mu = 0$ (i.e., Fermi wavevector $k_F = 0$) and $m = 0.5\lambda$. $R/a = 40$ in panel (d).

$$\text{Det}\begin{pmatrix} i & \lambda(q_z + iq_x) & \lambda(-q_z + iq_x) & 0 \\ -\eta & M_\eta(k_y) - E & M_\eta(k_y) - E & 0 \\ 0 & \lambda(q_z + iq_x)e^{iq_z L_z} & \lambda(-q_z + iq_x)e^{-iq_z L_z} & i \\ 0 & (M_\eta(k_y) - E)e^{iq_z L_z} & (M_\eta(k_y) - E)e^{-iq_z L_z} & \eta \end{pmatrix} = 0. \tag{11}$$

Simplifying this condition, we obtain a transcendental equation,

$$\frac{\tanh\left(L_z\sqrt{(M_\eta/\lambda)^2 - \chi}\right)}{L_z\sqrt{(M_\eta/\lambda)^2 - \chi}} = -\frac{\lambda}{L_z\eta M_\eta}, \tag{12}$$

where $\chi = (E/\lambda)^2 - q_x^2$. For all real solutions χ of this equation, the energy has values $E = \pm\lambda\sqrt{\chi + q_x^2}$. No solutions of Eq. 12 exist with $\chi < 0$.

For bound-state solutions, i.e, when q_z is imaginary, $\chi < (M_\eta/\lambda)^2$. The left hand side of Eq. 12 is a positive function with values between 0 and 1. Thus, such bound-state solutions are only possible when $\eta M_\eta < 0$ as well as when $|L_z M_\eta/\lambda| > 1$, i.e., when $|M_\eta| > \lambda/L_z$. Defining $\chi' = L_z^2\chi$ and $M'_\eta = \eta L_z M_\eta/\lambda$, we rewrite Eq. 12 as

$$\frac{\tanh(\sqrt{M_\eta'^2 - \chi'})}{\sqrt{M_\eta'^2 - \chi'}} = -\frac{1}{M'_\eta}. \tag{13}$$

The various solutions of χ' from Eq. 13 can be labeled by an index $n = 0, 1, ..$ (with increasing values of n corresponding to larger values of χ') and the corresponding energy solutions $E_{n,\pm}(q_x, q_y) = \pm\lambda\sqrt{\chi_n + q_x^2}$ gives rise to particle-hole symmetric bands. The minimum solution of χ' is shown in Fig. 2. The bands with $n = 0$ contain all the Fermi arc states (when k_y is between the Weyl nodes, in the Fermi arc interval) as well as low-energy bulk states (when k_y is outside the interval).

The a, b coefficients in Eq. (10), can be found from the

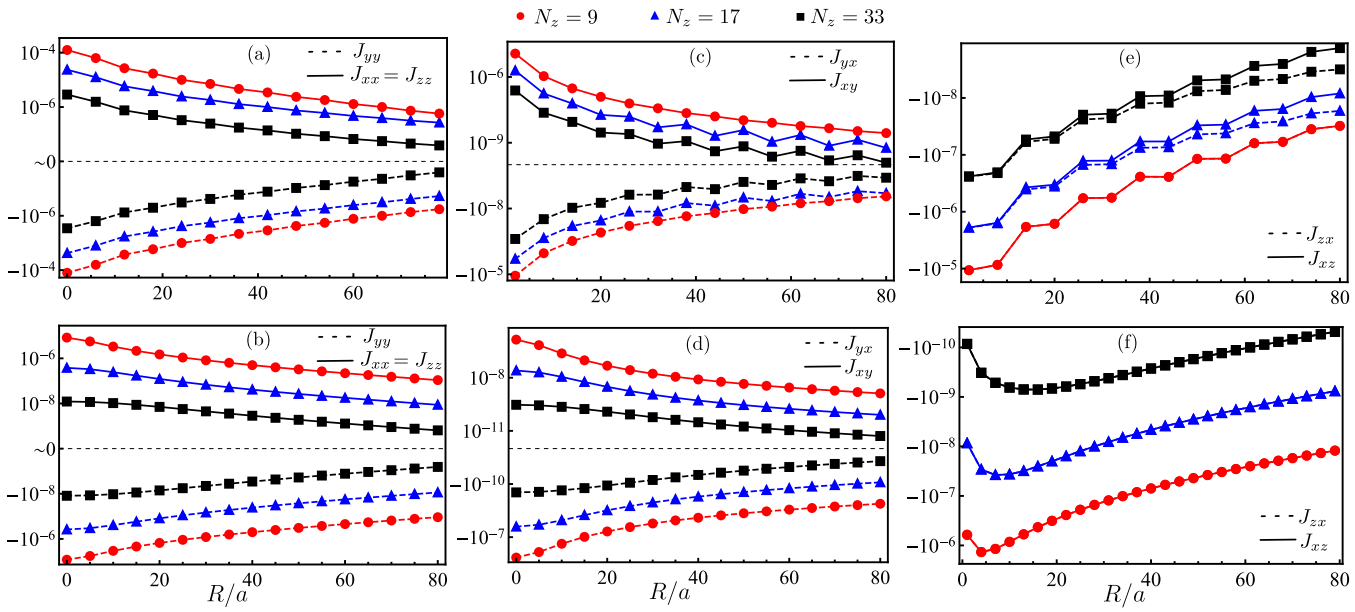

FIG. 4. The RKKY coupling between two spins (connected to same orbital) on opposite surfaces of the WSM slab, with the positions of the two spins at $(x, y, z) = (0, 0, 0)$ and $(R, 0, L_z = N_z a)$. (a), (c) and (e) are results for the analytical wavefunctions keeping only the $n = 0$ bands. (b), (d) and (f) show numerically evaluated results from the Green's function approach. With increasing thickness, all components decrease rapidly (shown in more detail in Fig. 5 and tabulated in Table II). These results are for $\mu = 0$ ($k_F = 0$). For all panels, $m = 0.5\ \lambda$.

boundary conditions at $z = 0$ to be

$$\frac{a}{b} = -\frac{M_\eta - E + \eta\lambda(q_x + iq_z)}{M_\eta - E + \eta\lambda(q_x - iq_z)}. \tag{14}$$

We can then write down the wavefunctions. Defining $K = M_\eta(k_y) - E, f = \lambda(q_x - iq_z), g = \lambda(q_x + iq_z)$, one finds

$$|\psi\rangle = \frac{1}{\sqrt{N}}\left\{(K + \eta g)\begin{pmatrix} if \\ K \end{pmatrix} e^{iq_z z} + (K + \eta f)\begin{pmatrix} -ig \\ -K \end{pmatrix} e^{-iq_z z}\right\}. \tag{15}$$

For real $q_z = \sqrt{\chi - M_\eta(k_y)^2}$ (when $\chi > m^2$, $f = g^*$) the normalization factor has the form

$$N = 2|K + \eta f|^2(K^2 + |f|^2)L + \mathrm{Im}\left[(K + \eta f)^2(K^2 + g^2)\left(\frac{e^{-2iLq_z} - 1}{q_z}\right)\right]. \tag{16}$$

For purely imaginary $q_z = i\kappa$ (when $\chi < m^2$),$f = q_x + \kappa$, $g = q_x - \kappa$,

$$N = -2(K + \eta f)(K + \eta g)(K^2 + gf)L + [(K + \eta g)^2(f^2 + K^2)e^{-\kappa L} + (K + \eta f)^2(g^2 + K^2)e^{\kappa L}]\frac{\sinh(\kappa L)}{\kappa}. \tag{17}$$

These are the full solutions of the low-energy states of the WSM slab in the rotated basis (Eq. (2)). Once written in the original basis, these solutions correctly reproduce the spin configuration of the Fermi arc states.

In what follows, we retain only the $n = 0$ wavefunctions above to calculate the one and two surface surface Green's functions. Using the unitary transformation U, we then write these Green's functions in the original basis of our model Hamiltonian to compute the RKKY couplings.

III. RKKY INTERACTION AND RECURSIVE GREEN'S FUNCTION

Ruderman-Kittel-Kasuya-Yoshida (RKKY) theory[2] describes the effective coupling between two impurity spins $\mathbf{S}_1$ and $\mathbf{S}_2$ in a metal mediated by the conduction electrons. The spins, located respectively at $\mathbf{r}_1$ and $\mathbf{r}_2$, are typically treated as classical magnetic moments, and are assumed to be coupled to the electrons by *sd* Hamiltonians, $H_{sd} = J\mathbf{S}_i \cdot \mathbf{s}(\mathbf{r}_i)$ $(i = 1, 2)$, where $\mathbf{s}(\mathbf{r}_i)$ is the conduction electron spin density at the location of impurity spin i. For small $\mathcal{J}$, the resulting impurity spin interaction becomes

$$H_{\mathrm{RKKY}} = -\frac{\mathcal{J}^2}{\pi}\int_{-\infty}^{E_F} d\omega \mathrm{Tr}[(\mathbf{S}_1.\mathbf{s})G(\mathbf{r}_{12}; \omega + i0+)(\mathbf{S}_2.\mathbf{s}) \times G(-\mathbf{r}_{12}; \omega + i0+)] \tag{18}$$

$$\equiv \sum_{i,j=x,y,z} J_{ij} S_{1i} S_{2j}, \tag{19}$$

where $\mathbf{r}_{12}$ is the separation of the two spins and $G(\mathbf{r}_{12};\omega+i0+)$ is the real space Green's function for the unperturbed electron system. The resultant J_{ij} is essentially the electronic spin-spin correlation matrix. In all of our results we show J_{ij} in units of $\mathcal{J}^2$.

Details of the particular electron system in which the impurity spins are embedded enter the calculation through $G(\mathbf{r}_{12};\omega+i0+)$. For our WSM system, we will proceed in two ways. First, we will directly compute G in momentum space from the low-energy Hamiltonian wavefunctions Eq. (15), and then Fourier transform the expression to obtain the needed real-space Green's function. Our second approach is more numerical, and involves inverting the tight-binding model, Eq. (1). In this approach the discrete translational invariance in the $x-y$ plane of the slab geometry allows, for each two dimensional wavevector, independent computation of the Green's function. A computation of the real space Green's function then follows from a Fourier transform. For the results we present in the next section, we also restrict ourselves to considering impurities which are exchange-coupled to the same orbital of the two-orbital model, Eq. 1, which captures the essential physics of interest. For the case of the semi-analytical model of the last section, for which the atomic-scale structure is not included, we assume the impurities to be exchange-coupled to the conduction electrons within a small region (of thickness of one lattice spacing) on each surface.

Before proceeding to our results, we use the remainder of this section to outline the recursive Green's function method we use for our fully numerical studies. We are interested in the coupling between impurities placed on the surfaces, so that in the computation of $G(\mathbf{r}_{12};\omega+i0+)$ one only actually needs the Green's function for sites $\mathbf{r}_1$ and $\mathbf{r}_2$ on the slab surfaces. Following Ref. 25, we can compute the two dimensional Fourier transform of this, $G_{ij}(\omega,k_x,k_y)$, where i and j label the surfaces of the slab on which $\mathbf{r}_1$ and $\mathbf{r}_2$ reside, respectively.

For a slab geometry of N_z number of sites in the z direction, we re-write the tight-binding Hamiltonian (Eq. 1) in the form

$$H(\vec{k}_{||}) = \sum_j \Big(\psi_j^\dagger(\vec{k}_{||}) A(\vec{k}_{||}) \psi_{j+1}(\vec{k}_{||}) + \text{h.c.} + \psi_j^\dagger(\vec{k}_{||}) h_{j,j}(\vec{k}_{||}) \psi_j(\vec{k}_{||}) \Big), \tag{20}$$

where $\vec{k}_{||} = (k_x, k_y)$, which are good quantum numbers. This allows us to write the Hamiltonian in the form of

$$H = \begin{pmatrix} h & A & 0 & . & 0 \\ A^\dagger & h & A & . & 0 \\ 0 & A^\dagger & h & . & 0 \\ . & . & . & . & . \\ 0 & 0 & 0 & . & h \end{pmatrix} \tag{21}$$

and the Green's function is evaluated from the equation

$$\Big(\omega\mathbb{I} - H(\vec{k}_{||})\Big)\, G(\vec{k}_{||},\omega) = \mathbb{I}. \tag{22}$$

When $N_z = 1 + 2^k$, the above set of equations can be recast in the form

$$(\omega\mathbb{I} - h')\, G' = \mathbb{I}, \tag{23}$$

with

$$h' = \begin{pmatrix} h^{(k)} & A^{(k)} \\ A^{\dagger(k)} & h^{(k)} \end{pmatrix}, \quad G' = \begin{pmatrix} G_{11} & G_{1N_z} \\ G_{N_z1} & G_{N_zN_z} \end{pmatrix}, \tag{24}$$

where the $h_t^{(k)}, h_b^{(k)}$ and $A^{(k)}$ are found by recursively solving

$$\begin{aligned} A^{(i+1)} &= A^{(i)}(\omega - h^{(0)})^{-1} A^{(i)}, \\ h^{(i+1)} &= h^{(i)} + A^{\dagger(i)}(\omega - h^{(i)}) A^{(i)} + A^{(i)}(\omega - h^{(i)}) A^{\dagger(i)}, \\ h_t^{(i+1)} &= h_t^{(i)} + A^{(i)}(\omega - h^{(i)})^{-1} A^{\dagger(i)}, \\ h_b^{(i+1)} &= h_b^{(i)} + A^{\dagger(i)}(\omega - h^{(i)})^{-1} A^{(i)}, \end{aligned} \tag{25}$$

with $h_t^{(0)} = h_b^{(0)} = h^{(0)} = h$ and $A^{(0)} = A$. This yields the two surface Green's functions $G(\vec{k}_{||})_{1,1}$ and $G(\vec{k}_{||})_{N_z,N_z}$ as well as their connections $G(\vec{k}_{||})_{1,N_z}$ and $G(\vec{k}_{||})_{N_z,1}$ without requiring a solution for the full Green's function.

IV. NUMERICAL RESULTS

In this section, we present our results for the specific cases when (*i*) the magnetic impurities are on the same surface of the WSM, and (*ii*) when the magnetic impurities are on opposite surfaces of the WSM. In both cases we compute the RKKY interaction using the recursive Green's function method outlined in the last section, as well as using the analytical wavefunctions of the $n = 0$ bands of Sec. II, which contain the Fermi arc states, and compare the results.

A. Impurities on a single surface

As discussed above, the Fermi arc states disperse in energy along $\vec{k}$ perpendicular to the arc itself. As a result these states have a highly asymmetric velocity, with $v_y \ll v_x$. The effective interaction between spin impurities placed on the same surface reflects this strong asymmetry. For a semi-infinite system, it can be shown for large r that the elements of the Green's function $G(\vec{r})$ asymptotically vanish as $\sim 1/r^2$ when $\vec{r}$ is on the surface and $\vec{r} \parallel \hat{y}$. By contrast, they fall off as $\sim 1/r$ when $\vec{r}$ points along the $\hat{x}$ direction[21]; the difference is a consequence of the (nearly) unidirectional dispersion of the Fermi arc energies. This results in the strongest RKKY coupling for impurities separated along the $\hat{x}$ direction, and in what follows we focus on separations along this direction. Moreover, for a thick enough sample (when the presence of the other surface may be neglected), states

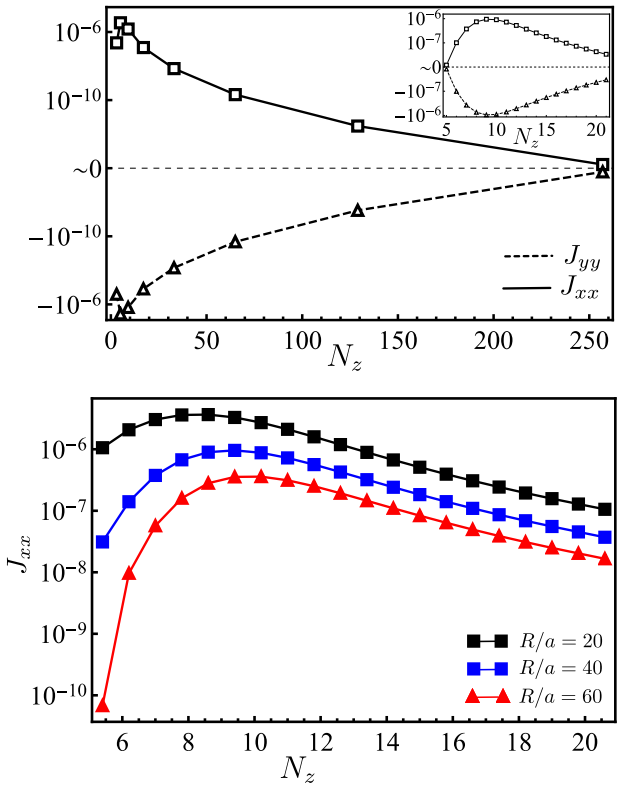

FIG. 5. Top main panel: The RKKY coupling between two spins (connected to same orbital) on opposite surfaces of the WSM slab of thickness $L_z = N_z a$ and placed at (0,0,0) and $(R = 40a, 0, L_z)$ as a function of N_z, evaluated using numerical Green's function method. Inset: Results from analytical wavefunctions, keeping only the $n = 0$ bands. With increasing thickness, all components of RKKY coupling decrease rapidly after attaining a maximum value at an optimum thickness (see discussion in the main text). Bottom panel: The RKKY coupling between two spins (connected to same orbital) on opposite surfaces of the WSM slab of thickness $N_z a$ placed at three lateral distances $(R = 20a, 0, L_z)$, $(R = 40a, 0, L_z)$, $(R = 60a, 0, L_z)$ as a function of N_z. These results are computed using the analytical wavefunctions keeping only the $n = 0$ bands. Note that the spin-spin couplings peak at slightly different slab thickness for different lateral separations between them and $J_{xx} = J_{yy} \approx -J_{zz}$. Other parameters are same as in Fig. 4.

in each of the Fermi arcs are spin-polarized (along the direction of σ_x in our model) and are chiral in their dispersion (i.e, the energy is proportional to $\pm k_x$ for $\eta = \pm 1$). For such helical states, where oppositely polarized electrons move in opposite directions, one expects the spin-spin coupling will vanish for the impurities with spin-polarization parallel to that of the electrons[5,17,21]. This argument suggests that J_{xx} will vanish for coupling among spins mediated by a single Fermi arc.

These expectations may be understood as follows. The Fermi arcs, for a thick sample, are exponentially confined to a surface at $z = 0$ with an approximate wave function (see Eqs (7) and (8))

$$\psi_{\rm FA}(\mathbf{r}) \approx e^{ik_x x} e^{ik_y y} e^{-|M_\eta(k_y)|\frac{z}{\lambda}} \begin{pmatrix} i \\ -\eta \end{pmatrix}, \qquad (26)$$

where $M_\eta(k_y) = m\eta - \lambda \sin(k_y)$. These wavefunctions allow us to write an effective Green's function from the Fermi arc on this two-dimensional surface in the form

$$G^{\rm FA}_\eta(\omega + i\delta; \mathbf{r}) = (\sigma_0 - \eta\sigma_y) \int \frac{d^2k}{(2\pi)^2} \frac{e^{ik_x x} e^{ik_y y}}{\omega - \eta v_F k_x + i\delta} \times \frac{|M_\eta(k_y)|}{\lambda} \theta(k_y - k_{\eta,1}) \theta(k_{\eta,2} - k_y), \qquad (27)$$

where the Fermi arcs exist between $k_{\eta,1} = \eta\frac{\pi}{2} - k_0$ and $k_{\eta,2} = \eta\frac{\pi}{2} + k_0$. The k_y momentum can be integrated between $k_{\eta,1}$ and $k_{\eta,2}$ and performing the k_x integral one obtains,

$$G^{\rm FA}_\eta(\omega + i\delta; \boldsymbol{r}) = i \frac{\sigma_0 - \eta\sigma_y}{\pi v_F^2} e^{i(\omega + i\delta)\frac{|x|}{v_F}} I(y) \theta(\eta x), \qquad (28)$$

where, the Fermi velocities of the Weyl nodes $v_F = \lambda$. In the limit $\delta \to 0+$,

$$I(y) = e^{i\pi y/2} \Gamma(y), \qquad (29)$$

$$\text{with} \quad \Gamma(y) = \frac{m \sin(yk_0) - y\lambda \sin k_0 \cos(yk_0)}{y(y^2 - 1)}, \qquad (30)$$

and $\boldsymbol{r} = (x, y)$. This approximate form for the Green's function is useful in determining the asymptotic behavior of the RKKY interaction, as we show briefly in the next section (see also Ref. 21). Note that the step function in Eq. (28) implements the chiralities of the Fermi arcs. As $\eta = \pm$, in the full 4×4 orbital/spin space, the Green's function is then

$$G^{\rm FA}(\omega; \mathbf{r}) = \begin{pmatrix} G^{\rm FA}_+(\omega; \mathbf{r}) & 0 \\ 0 & G^{\rm FA}_-(\omega; \mathbf{r}) \end{pmatrix}. \qquad (31)$$

With this expression it is straightforward to work out the RKKY integral (Eq. 18) and show that, in the original basis of the Hamiltonian, Eq. (1), the elements of the correlation matrix, Eq. (19), are given by

$$J_{xx} = 0; \quad J_{yy} = J_{zz} = -\frac{J^2 \Gamma(y)^2}{2\pi^3 v_F^3 x} \cos(2k_F x + \pi y), \qquad (32)$$

$$J_{zy} = -J_{yz} = \frac{J^2 \Gamma(y)^2}{2\pi^3 v_F^3 x} \sin(2k_F x + \pi y). \qquad (33)$$

Other off-diagonal components vanish. In this limit, the separation of the *pairs* of the Weyl nodes (taken as π/a in our model) does not alter the result. Note that a non-vanishing asymmetric Dzyaloshinskii-Moriya (DM)[26,27] type of exchange interaction ($J_{zy} = -J_{yz} \neq 0$) arises among the impurity spins due to the broken inversion symmetry of the system. The symmetries apparent in Eqs. 33 can be understood from the original tight-binding system, as we discuss in Appendix A. These are reflected in our results, as illustrated in Fig. 3.

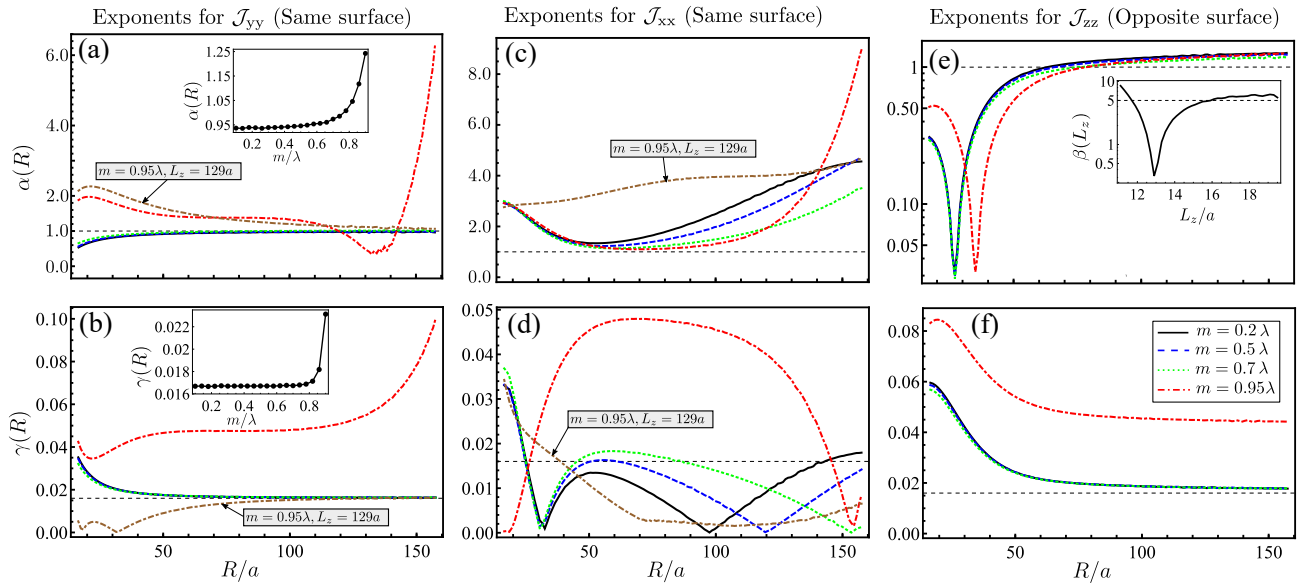

FIG. 6. **Asymptotic behavior of spin-spin couplings:** (color online) Exponents α, γ and β (see the main text) of the RKKY coupling between the two spins are estimated for various values of the parameter m/λ, where a larger m/λ ratio represents a smaller length of the Fermi arc in the momentum space, which is given by $2\cos^{-1}(m/\lambda)$. All other figures of the coupling amplitudes, in the main text, are shown for $m/\lambda = 0.5$. (a) to (d) shows the exponents when the spins are on the same surface, and (e), (f) shows the exponents when the two spins are on the opposite surfaces. Other than the plots for larger thickness, which are marked directly in the sub-figures (a)-(d), the thickness of the sample is kept fixed at $L_z = 33a$ for all of the cases. Linearly dispersing electronic states would result in $\gamma = 2\delta/\lambda \approx 0.016$, where δ is the small imaginary part added to the denominator of the Green's function. Plots for which $\gamma \approx 2\delta$ imply that the electronic states most important in the coupling are linearly dispersing. In the inset of (a) and (b), we show the behavior of α and γ parameters for the spins on the same surface by varying m/λ continuously for a fixed separation of the spins, $R = 80a$. In the inset of (e), we show the nature of the parameter β for spins on opposite surfaces by varying m/λ continuously for a fixed in-plane separation of the spins, $R = 40a$.

In particular the value of J_{xx} attains a maximum at an optimum thickness $L_z = L_c$ and decreases with further increase in the thickness of the sample. The other components increase with increasing thickness and become constant as $L_z > L_c$, as shown in Fig. 3(d). In section C, we provide a detail analysis of asymptotic behavior of J_{xx} and J_{yy} for large R. Off-diagonal components other than J_{zy} and J_{yz} (not shown) are several orders of magnitude smaller than these quantities, as expected from the above analysis. (Note also the qualitative agreement between results from our semi-analytical model and the tight-binding computation.) The DM type of couplings follow similar behavior as that of J_{yy}. In Fig. 3(a), one sees $|J_{xx}| \ll |J_{yy}|, |J_{zz}|$, both for our numerical analysis (see below) and when using the analytical model with just the $n = 0$ band. However, J_{xx} shows further oscillations for the analytical model for larger values of N_z. The precise reason for this is uncertain; it may be caused either by limitations in our numerics, or due to the fact that the $n = 0$ band itself is not enough to fully capture the inter-surface coupling through the bulk states at larger thickness.

The results for J_{xx} obtained from the tight-binding computation are particularly interesting. If the coupling between the spins were only mediated by the Fermi arc states and if they are fully spin-polarized along $x-$direction, then one would expect J_{xx} to vanish. In contrast, in the slab geometry J_{xx} remains non-zero and falls off rather slowly (see Fig. 3) with the distance between the impurity spins. (Similar behavior is found in our analytical model at small thickness.) The discrepancy can be attributed to two possible effects: (i) interactions mediated by the bulk states which were not included in the simple Fermi arc analysis, and (ii) the presence of the second surface. Interestingly, Fig. 3(b) shows that J_{xx}, after attaining a maximum value, vanishes rapidly with increasing thickness, which clearly favors mechanism (ii). Indeed, the non-monotonic behavior of J_{xx} can be understood as follows. Initially when the sample thickness is small, processes that couple the spins involve both surfaces, which host states of opposite helicity. The surface density of states increases with increasing thickness, giving rise to values of J_{xx} that increase with thickness. At larger thicknesses, the second surface becomes increasingly inaccessible to impurities on the first surface. Thus J_{xx} deceases rapidly with further increase in thickness. Since the chiral nature of the surface states does not affect the other RKKY couplings, with rising sample thickness these couplings increase monotonically, due to the increasing surface density of states.

They saturate to constant values at large thickness.

The critical thickness L_c can be used to define a "thin-film limit" of the system, for which the effects of having two surfaces are maximal. Noting that k_0 is the only relevant momentum scale, we expect the thin film limit to scale as $L_c \sim a/k_0$. A numerical verification of this hypothesis is presented in Appendix B.

B. Impurities on opposite surfaces

When the impurity spins are put on opposite surfaces of the slab, they may communicate via electron states that are present in the bulk of the Weyl semimetal. To examine this effect numerically, we place the two spins on different surfaces of a WSM slab with various thicknesses and vary their separation along the x axis (i.e., the direction in which the Fermi arcs states disperse). Results from these are illustrated in Figs. 4 and 5.

For the range of parameters we examined, the symmetry properties of the spin coupling matrix turn out to be the same as when the spins are situated in the bulk and are separated along the z direction (see Appendix A). Numerically, when the two spins are located at sites $(x, y, z) = (0, 0, 0)$ and $(R, 0, L_z = N_z a)$, the coupling between them is surprisingly strong despite the fact that they reside on different surfaces. It is shown in Fig. 4 that in addition to DM-type exchange couplings, symmetric off-diagonal type[27] exchange couplings $J_{xz} = J_{zx}$ are also present. The asymptotic behavior of diagonal couplings for large R are discussed in detail in Section C below; off-diagonal components of the coupling matrix have asymptotic behavior similar to diagonal components.

As a function of the thickness L_z, for fixed R all the couplings initially increase and after attaining maximum values decrease rapidly. Results for both the analytical and tight-binding approaches for varying N_z are illustrated in Fig. 5. The non-monotonic behavior of all the couplings as a function of thickness can be qualitatively understood as follows. As the thickness increases, the Fermi arcs localize increasingly firmly on the surfaces, increasing the surface density of states near the Fermi energy. This leads to an increase in the coupling between the impurity spins on the surfaces and the conduction electrons, which can mediate intersurface interactions effectively when L_z is not too large. On the other hand, as L_z increases, the number of conduction electron states which are sensitive to both surfaces decreases, resulting in weaker coupling between spins on opposite surfaces. With increasing thickness, the competition between these two mechanisms gives rise to a critical thickness for which the coupling between spins placed on opposite surfaces maximizes. As in our earlier argument for impurities on the same surface, with k_0 the only relevant momentum scale we expect this thickness to scale as $\sim a/k_0$. We explore this in Appendix B. Again this critical thickness also defines a thin-film limit; the values of this critical thickness obtained from inter-surface coupling are of the same scale as those obtained from the intra-surface coupling.

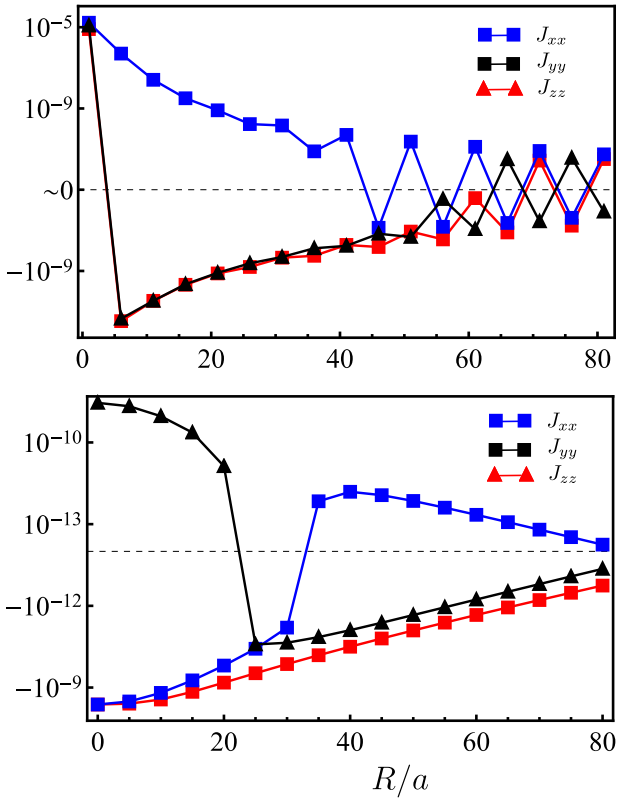

FIG. 7. RKKY coupling for slab with surfaces perpendicular to the inter-Weyl node separation (y direction in our model) for which there are no Fermi arcs. $m = 0.5\lambda$, $N_z = 33$. Top panel: Spins on the same surface. Bottom panel: Spins on opposite surfaces. In comparison with Figs. 3 and 4 the couplings are very small. For larger R, as the J_{ii} become very small, the oscillations are likely due to the numerical inaccuracy.

C. Asymptotic Behavior

In this section we analyse the asymptotic behavior of RKKY couplings based on the observations shown in Figs. 3, 4, 5. We first examine the behavior of the various RKKY couplings as the distance between spin impurities becomes very large. For numerical estimation of the functional form of the J_{ii} as $\mathbf{R}$ along $\hat{x}$ becomes large, we numerically evaluate two quantities,

$$\alpha(R) = R^2 \frac{d^2 \log J}{dR^2}, \gamma(R) = -a \frac{d}{dR}\left(R \frac{d \log J}{dR}\right), \quad (34)$$

and plot them as function of R in Fig. 6(a)-(d). Essentially, if these functions become independent of R at large R, then the asymptotic functional form of the coupling is $J \sim e^{-\gamma(R/a)} R^{-\alpha}$. The numerical origin of γ is that in

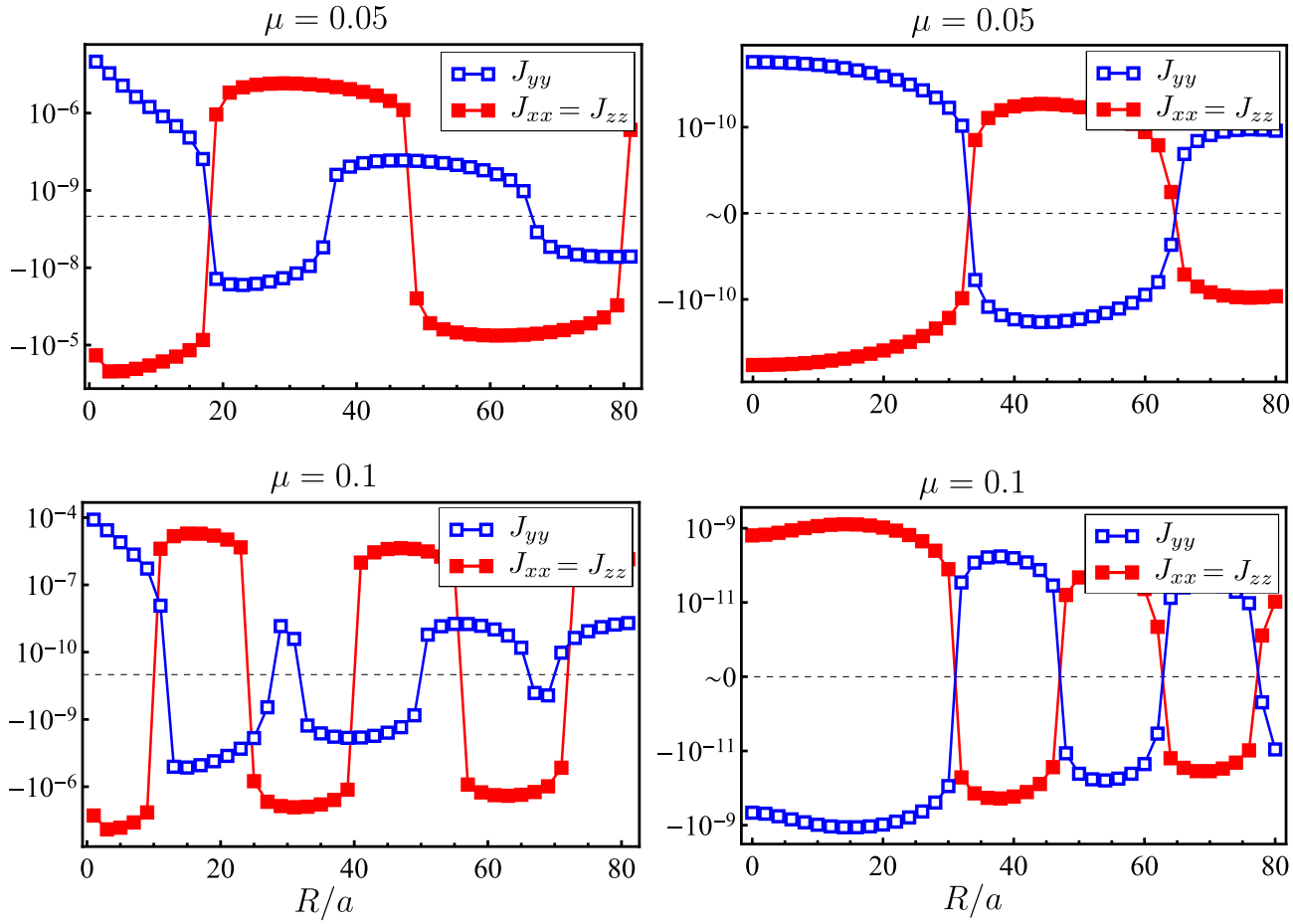

FIG. 8. The diagonal elements of coupling matrix at a finite chemical potential (given by μ in units of λ), showing $2k_F$ oscillations. The left column shows the results for the spins on the same surface of the slab and the right column shows the results when the spins are on opposite surfaces. The slab thickness $N_z = 33$ and all other parameters are same as in Figs. 3 and 4.

evaluating the Green's function, we add a small imaginary value δ to ω, which models contacting the electrons to some source of incoherence. For a system with linear dispersion, it is easy to check that the resulting γ in the asymptotic limit would simply be 2δ, which matches well with the numerically estimated value of γ for J_{yy} and J_{zz}. As $\delta \to 0$, γ should also vanish.

The separation of Weyl nodes in momentum space is controlled by the parameter m/λ and is given by $2\cos^{-1}(m/\lambda)$. As shown in Fig. (6), for all values of possible Weyl node separations, the numerical estimation of α indicates that $J_{zz}, J_{yy} \sim 1/R$ for $R \gg a$. For very small separation of the Weyl nodes (i.e, for m/λ close to unity) convergent $1/R$ behavior is reached only for a large thickness. Note that, at very large R (such that $k_0 R/a \gg 1$), it is predicted that J_{zz} and J_{yy} would fall off asymptotically roughly as $1/R^2$ due to the curvature of the Fermi arcs[21]. Our numerical results suggest that Fermi arc curvature effects on the exponent may require very large spin separations to become noticeable.

Our estimate of the quantities α and γ display a surprisingly slow decay of the coupling with impurity separation, even for spins on opposite surfaces. This raises the possibility that magnetizations on the surfaces should order at low temperature. For intersurface coupling, γ remains close to 2δ for large R, but $\alpha(R)$, even for large R, shows a weak R dependence, hinting that the coupling may have a more complicated asymptotic form that $1/R$. Our numerical estimate of $\alpha(R)$ for a large R ($\approx 150a$) is about 1.25. Results from the tight-binding simulation and from the low-energy wavefunctions both support this result.

In the inset of Fig. 6(e), we plot the function

$$\beta(L_z) = L_z^2 \frac{d^2 \log J}{dL_z^2} \tag{35}$$

as a function of L_z using the results from the low-energy wavefunctions (for fixed R), showing that at large L_z, β retains a value ≈ 5. Thus as a function of thickness, the coupling decays as $\sim e^{-\tilde{\gamma}(L_z/a)} L_z^{-\beta}$ with $\beta \approx 5$. This value of β matches the power-law falloff of RKKY coupling for spins in the bulk of the WSM[18,21], suggesting that for large enough L_z the coupling between spins on

opposite surfaces is dominated by the bulk states. The coefficient $\tilde{\gamma}$ (not shown) arises due to the non-vanishing δ.

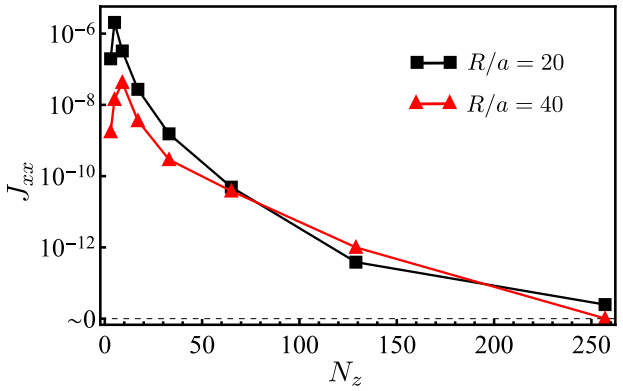

FIG. 9. The J_{xx} coupling between spins on opposite surfaces for the system with a finite but small chemical potential $\mu/\lambda = 0.05$, as a function of the thickness of the slab, showing that the non-monotonic behavior persists (compare to figure 5, where the chemical potential is the energy of the Weyl nodes). Other parameters are the same as in Fig. 5. Other couplings behave analogously.

V. SUMMARY AND DISCUSSION

In this work we have examined RKKY interactions among impurity spins on the surfaces of Weyl semimetal (WSM) slabs, using both an approach in which the wavefunctions of the WSM electrons are found in an analytical form, and a more fully numerical recursive Green's function technique. We find that Fermi arc surface states play an important role in the RKKY coupling, creating couplings that are stronger and more long-range than is found for impurities well-inside the bulk of the system. Surprisingly, even the coupling between spins on opposite surfaces can be relatively strong. As a function of film thickness, we find that the RKKY couplings are non-monotonic, with maxima that can define a "thin-film" limit, in which the effects of *both* surfaces are in some sense maximal. The relative strengths and signs of different components of the RKKY couplings J_{ij} can be understood using a simple model in which only surface states associated with the Fermi arcs are retained, and in which the Fermi arcs are perfectly straight.

The importance of electron states with strong support on the surfaces can be examined by comparing results for geometries with Fermi arcs to ones without them. Fig. 7 illustrates RKKY coupling for spins on the same and opposite surfaces which are perpendicular to the direction of separation between the Weyl nodes in the bulk, for which surface states are not present. The generally smaller scale of the resulting couplings supports the idea that the Fermi arc states play a large quantitative role in setting the coupling scale.

The results presented to this point have been for vanishing chemical potential μ, where the only extended Fermi surfaces are due to the Fermi arcs, and the Fermi energy passes directly through the Weyl nodes in the bulk. In general, when $\mu \neq 0$ and the Fermi wavevector $k_F \neq 0$ in the bulk, one expects $2k_F$ oscillations in the RKKY coupling. Results for $\mu \neq 0$ are presented in Fig. 8, for which the oscillations are apparent. The envelopes within which these oscillations occur behave rather similarly to the results for $\mu = 0$. For finite, but small μ, the nonmonotonic behavior of the couplings that defines the "thin-film limit" persists, as illustrated in Fig. 9.

When a system is of order or thinner than a critical thickness $\sim 1/k_0$, our results show that a proper treatment of RKKY interactions requires one to retain states from the Fermi arcs of *both* surfaces, even if the two spins reside on the same surface. For real systems, such as TaAs[28], the typical separation of Weyl nodes is rather small (of the order of $k_0 \approx 0.1\pi/a$) and thus we expect the critical thickness to be of the order of several tens to a hundred lattice spacings. Such thicknesses are quite reasonable for thin-film semiconductor systems.

We conclude with some speculations about the kind of magnetic order these RKKY interactions might induce in the low temperature state of spin impurities on the surfaces of a WSM thin film. At large distances, the strongest couplings we find are for $J_{yy} = J_{zz} < 0$ within a single surface, suggesting the system will form a planar ferromagnet in its ground state. The non-vanishing J_{yz} and J_{zy} couplings if large enough could induce spiral order; while at short distances these can be larger than the diagonal elements, at long distances the latter are significantly larger. Given the relatively slow spatial decay of the RKKY interaction, it seems likely that the system will favor ferromagnetism. Furthermore, the sign of coupling for impurities on different surfaces suggests that the magnetization of the two surfaces will be parallel to one another in the groundstate. In principle at low temperature such magnetic order should be detectable. Moreover, with this type of order one expects a magnetic disordering transition at finite temperature in the Kosterlitz-Thouless universality class, which might be detected in thermal measurements or via spin transport in the system. Finally, the importance of the Fermi arc states in supporting such magnetic order could be tested by comparing the behavior of slabs in which the surfaces support them to ones in which they do not. We leave the investigation of these questions to future work.

Acknowledgements – This work is supported in part by the NSF through grant Nos. DMR-1506263, DMR-1914451, and ECCS-1936406. Further support was supplied by the US-Israel Binational Science Foundation grant No. 2016130. H.A.F. acknowledges the support of the Research Corporation for Science Advancement through a Cottrell SEED Award, and the hospitality and support of the the Aspen Center for Physics via NSF grant PHY-1607611, where parts of this work were performed. A.K. thanks SERB, DST (Gov. of India) and

BRNS, DAE (Gov. of India) for support through research grants. D.G. thanks support from Council of Scientific and Industrial Research (Gov. of India).

[1] For reviews see: N. P. Armitage, E. J. Mele, and A. Vishwanath, Rev. Mod. Phys. **90**, 015001 (2018); Nature S. Jia, S.-Y. Xu, and M. Z. Hasan, Nature Materials **15**, 11401144 (2016); S. Rao, Journal of the Indian Institute of Science, **96**, 2 (2016).

[2] M. A. Ruderman and C. Kittel, Phys. Rev. **96**, 99 (1954); T. Kasuya, Prog. Theor. Phys. **16**, 45 (1956); K. Yosida, Phys. Rev. **106**, 893 (1957).

[3] H. Imamura, P. Bruno, and Y. Utsumi, Phys. Rev. B **69**, 121303(R) (2004).

[4] A. Schulz, A. DeMartino, P. Ingenhoven, and R. Egger, Phys. Rev. B **79**, 205432 (2009).

[5] J. Gao, W. Chen, X. C. Xie, and F.C. Zhang, Phys. Rev. B **80**, 241302(R) (2009).

[6] Q. Liu, C.-X. Liu, C. Xu, X.-L. Qi, and S.-C. Zhang, Phys. Rev. Lett. **102**, 156603 (2009).

[7] M. Sherafati and S. Satpathy, Phys. Rev. B **83**, 165425 (2011).

[8] E. Kogan, Phys. Rev. B **84**, 115119 (2011).

[9] D. Mastrogiuseppe, N. Sandler, and S. E. Ulloa, Phys. Rev. B **93**, 094433 (2016).

[10] M. Zare, F. Parhizgar, and R. Asgari, Phys. Rev. B **94**, 045443 (2016).

[11] G. Yang, C.-H. Hsu, P. Stano, J. Klinovaja, and D. Loss, Phys. Rev. B **93**, 075301 (2016).

[12] C.-H. Hsu, P. Stano, J. Klinovaja, and D. Loss, Phys. Rev. B **96**, 081405(R) (2017).

[13] C.-H. Hsu, P. Stano, J. Klinovaja, and D. Loss, Phys. Rev. B**97**, 125432 (2018).

[14] Y.-W. Lee and Y.-L. Lee, Phys. Rev. B **91**, 214431 (20015).

[15] S. Reja, H.A. Fertig, L. Brey, and S. Zhang, Phys. Rev. B **96**, 201111(R) (2017).

[16] S. Reja, H.A. Fertig, and L. Brey, Phys. Rev. B **99**, 045427 (2019).

[17] Sonu Verma and Arijit Kundu, Phys. Rev. B **99**, 121409(R) (2019).

[18] H.-R. Chang, J. Zhou, S.-X. Wang, W.-Y. Shan, and D. Xiao, Phys. Rev. B **92**, 241103(R) (2015).

[19] Yong Sun and Anmin Wang, J. Phys.: Condens. Matter **29**, 435306 (2017).

[20] Mir Vahid Hosseini and Mehdi Askari, Phys. Rev. B **92**, 224435 (2015).

[21] V. Kaladzhyan, A. A. Zyuzin, and P. Simon, Phys. Rev. B **99**, 165302 (2019).

[22] Hou-Jian Duan, Shi-Han Zheng, Pei-Hao Fu, Rui-Qiang Wang, Jun-Feng Liu, Guang-Hui Wang, and Mou Yang, New J. Phys. **20**, 103008 (2018).

[23] Da Ma, Hua Chen, Haiwen Liu, and X. C. Xie, Phys. Rev. B **97**, 045148 (2018).

[24] M. M. Vazifeh and M. Franz, Phys. Rev. Lett. 111, 027201 (2013).

[25] K. Pareek and A. Kundu, arXiv:1812.05504 (unpublished).

[26] I. Dzyaloshinskii, Phys. Chem. Solids **4**, 241255 (1958).

[27] T. Moriya Phys. Rev. **120**, 91 (1960).

[28] B. Q. Lv, H. M. Weng, B. B. Fu, X. P. Wang, H. Miao, J. Ma, P. Richard, X. C. Huang, L. X. Zhao, G. F. Chen, Z. Fang, X. Dai, T. Qian, and H. Ding, Phys. Rev. X **5**, 031013 (2015).

APPENDIX

A. SYMMETRIES AMONG THE SUSCEPTIBILITY MATRIX ELEMENTS

In this appendix we briefly discuss the symmetries among the various coupling elements J_{ij} for spins that are on the same or opposite surfaces, as well as in the bulk, based on the symmetry of the underlying Hamiltonian of the WSM.

First we consider the case when both spins, coupled to same orbital, are on the *same surface* of a WSM slab of thickness N_z with spatial separation $(x = R, 0, 0)$. The two Green's functions $G(\mathbf{r}_{12}, \omega)$ and $G(-\mathbf{r}_{12}, \omega)$ required to calculate the RKKY coupling between the spins for some arbitrary values of x and ω have the structures

$$G(\mathbf{r}_{12}, \omega) = \begin{pmatrix} s_0 & s_1 & s_2 & s_3 \\ s_1 & s_0 & s_4 & s_2 \\ s_2 & -s_3 & s_0 & s_1 \\ -s_4 & s_2 & s_1 & s_0 \end{pmatrix}, \tag{36}$$

$$G(-\mathbf{r}_{12}, \omega) = \begin{pmatrix} s_0 & -s_1 & -s_2 & s_3 \\ -s_1 & s_0 & s_4 & -s_2 \\ -s_2 & -s_3 & s_0 & -s_1 \\ -s_4 & -s_2 & -s_1 & s_0 \end{pmatrix}, \tag{37}$$

where s_i (with $i = 0, 1, 2, 3, 4$) are complex numbers depending on R and ω. Using these in Eq. 19, we obtain all possible nonzero components of the spin-spin correlation matrix to be

$$\mathcal{J}_{zz} = \mathcal{J}_{yy},\ \mathcal{J}_{xx} \neq 0 \text{ and } \mathcal{J}_{zy} = -\mathcal{J}_{yz}. \tag{38}$$

Next, we consider the case when both spins, coupled to the same orbital, are on the *opposite surfaces* of WSM slab of thickness L_Z with lateral spatial separation R, the positions of the two spins are (0,0,0) and $(x = R, 0, L_z)$. The two Green's functions $G(\mathbf{r}_{12}, \omega)$ and $G(-\mathbf{r}_{12}, \omega)$ required to calculate the RKKY coupling between the spins for arbitrary values of R and ω now have the structure

$$G(\mathbf{r}_{12}, \omega) = \begin{pmatrix} o_0 & o_2 & 0 & o_3 \\ o_2 & o_1 & -o_3 & 0 \\ 0 & -o_3 & o_0 & o_2 \\ o_3 & 0 & o_2 & o_1 \end{pmatrix}, \tag{39}$$

$$G(-\mathbf{r}_{12}, \omega) = \begin{pmatrix} o_1 & -o_2 & 0 & o_3 \\ -o_2 & o_0 & -o_3 & 0 \\ 0 & -o_3 & o_1 & -o_2 \\ o_3 & 0 & -o_2 & o_0 \end{pmatrix}, \tag{40}$$

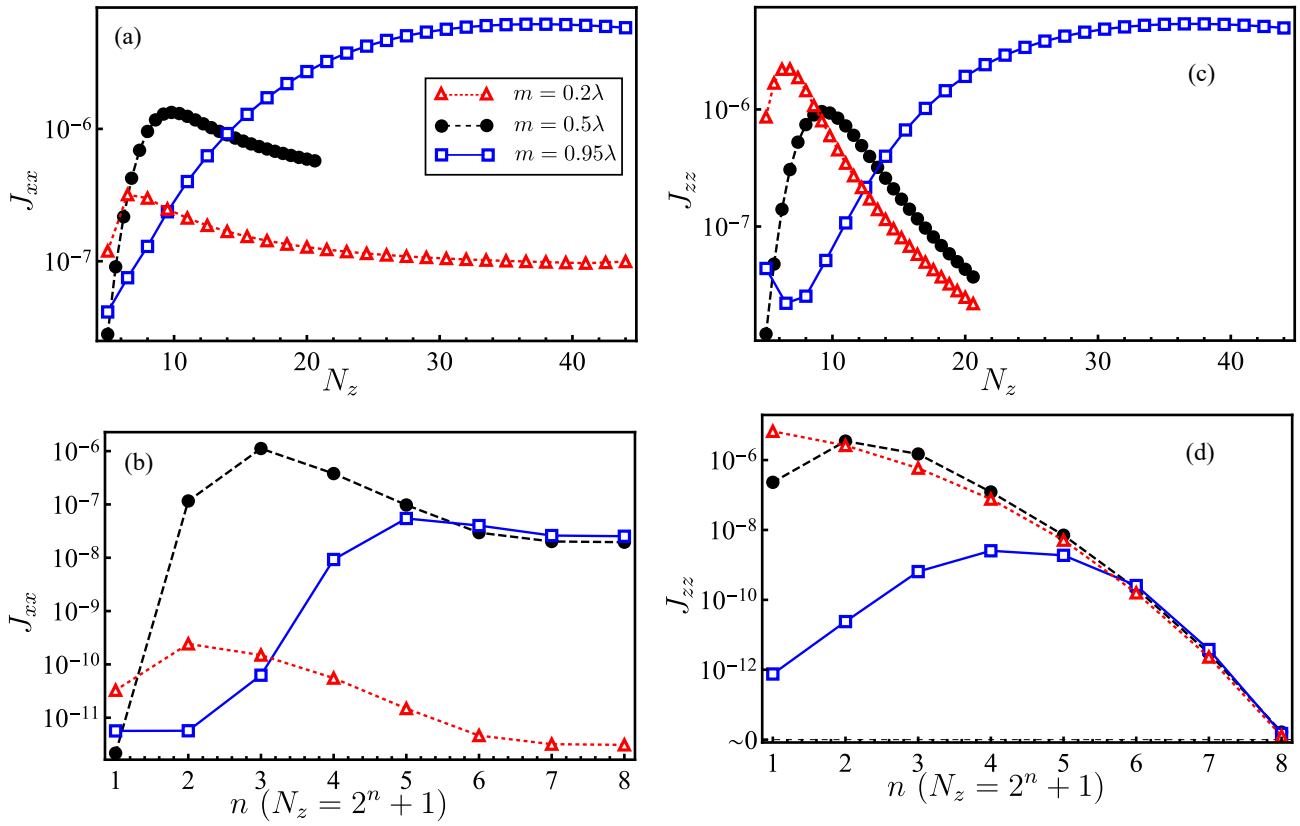

FIG. 10. The critical thickness at which the RKKY coupling is maximum depends strongly on the separation of the Weyl nodes in momentum space, given by $k_0 = \cos^{-1}(m/\lambda)$. For three values of $m/\lambda = 0.2$ (triangles), 0.5 (filled circles) and 0.95 (squares), (a) and (b) show the thickness dependence when the spins are on the same surface, while (c) and (d) show the thickness dependence when the spins are on opposite surfaces. For (a) and (c) the analytical solutions for wavefunctions of the low-energy Hamiltonian has been used. For (b) and (d) the recursive Green's function method was used directly on the tight-binding model. The parameter values are the same as for Figs. 3 and 4. For (a) and (b), the two spins are at positions $(x, y, z) = (0, 0, 0)$ and $(R = 40, 0, 0)$ and for (c) and (d) the two spins are at positions $(x, y, z) = (0, 0, 0)$ and $(R = 40, 0, L_z = N_z a)$.

with o_i (with $i = 0, 1, 2, 3, 4$) complex numbers depending on R, L_z, and ω (o_2 is two orders magnitude smaller than other elements). Using these in Eq. 19, we find all possible nonzero components of spin-spin correlation matrix are related by

$$\begin{aligned} &\mathcal{J}_{xx} \approx \mathcal{J}_{yy},\ \mathcal{J}_{zz} \neq 0\ ,\ \mathcal{J}_{xy} = -\mathcal{J}_{yx}, \\ &\mathcal{J}_{zx} = \mathcal{J}_{xz} \text{ and } \mathcal{J}_{zy} = -\mathcal{J}_{yz}. \end{aligned} \tag{41}$$

Finally, we consider the case when the two spins, coupled to the same orbital, are deep in the bulk of a WSM and have spatial separation $(0, 0, z = R)$. The two Green's functions $G(\mathbf{r}_{12}, \omega)$ and $G(-\mathbf{r}_{12}, \omega)$ required to calculate the RKKY coupling between the spins for some arbitrary values of R and ω have the structure

$$G(\mathbf{r}_{12}, \omega) = \begin{pmatrix} b_0 & 0 & 0 & b_2 \\ 0 & b_1 & -b_2 & 0 \\ 0 & -b_2 & b_0 & 0 \\ b_2 & 0 & 0 & b_1 \end{pmatrix}, \tag{42}$$

$$G(-\mathbf{r}_{12}, \omega) = \begin{pmatrix} b_1 & 0 & 0 & b_2 \\ 0 & b_0 & -b_2 & 0 \\ 0 & -b_2 & b_1 & 0 \\ b_2 & 0 & 0 & b_0 \end{pmatrix}, \tag{43}$$

where b_i, (with $i = 0, 1, 2, 3, 4$) are complex numbers depending on R and ω. Using these in Eq. 19, we obtain the components of the spin-spin correlation matrix as similar as those in Eqs. (41):

$$\begin{aligned} &\mathcal{J}_{xx} = \mathcal{J}_{yy},\ \mathcal{J}_{zz} \neq 0\ ,\ \mathcal{J}_{xy} = -\mathcal{J}_{yx}, \\ &\mathcal{J}_{zx} = \mathcal{J}_{xz} = 0 \text{ and } \mathcal{J}_{zy} = \mathcal{J}_{yz} = 0. \end{aligned} \tag{44}$$

B. CRITICAL THICKNESS AND THE SEPARATION OF THE WEYL NODES

Finally, we examine in more detail the k_0 dependence of the critical thicknesses at which the couplings are maximized, as discussed in the main text. Fig. 10 illustrates numerical results for the thickness dependence of RKKY couplings for various values of the Weyl node separation k_0, for both the cases when the spins are on the same surface as well as when the spins are on the opposite surfaces. If one estimates the critical thickness L_c at which the coupling attains its maximum, one finds that $L_c k_0/a \approx$ constant.